Journal of Petrology, 2024, **65**, 1–9
https://doi.org/10.1093/petrology/egae005
Advance access publication date 30 January 2024
Letter

Tracking Garnet Dissolution Kinetics in 3D Using Deep Learning Grain Shape Classification

Philip Hartmeier*, Pierre Lanari, Jacob B. Forshaw and Thorsten A. Markmann

Institute of Geological Sciences, University of Bern, Baltzerstrasse 3, 3012 Bern, Switzerland

*Corresponding author. E-mail: philip.hartmeier@students.unibe.ch

The kinetics of fluid-driven metamorphic reactions are challenging to study in nature because of the tendency of metamorphic systems to converge towards chemical equilibrium. However, in cases where mineral textures that reflect incomplete reactions are preserved, kinetic processes may be investigated. Atoll garnet, a texture formed by the dissolution of a garnet's core, has been described in 2D from thin sections of rocks worldwide. Quantifying the extent of this dissolution reaction requires a sample-wide examination of hundreds of individual grains in 3D. In this study, we quantified the distribution of atoll garnet using micro-computed tomography and grain shape analysis. A convolutional neural network was trained on human-labeled garnet grains for automated garnet classification. This approach was applied to a retrogressed mafic eclogite from the Zermatt–Saas Zone (Western Alps). Pervasive atoll-like resorption preferentially affected the larger porphyroblasts, suggesting that compositional zoning patterns exert a first-order control on dissolution rates. A kinetic model shows that the reactivity of metastable garnet to form atolls is favored at pressure–temperature conditions of 560 ± 30°C and 1.6 ± 0.2 GPa. These conditions coincide with the release of water when lawsonite breaks down during the exhumation of mafic eclogites. The model predicts dissolution rates that are three to five times faster for the garnet core than for the rim. This study shows that deep learning algorithms can perform automated textural analysis of crystal shapes in 3D and that these datasets have the potential to elucidate petrological processes, such as the kinetics of fluid-driven metamorphic reactions.

Key words: garnet; kinetics; machine learning; petrography; textures

INTRODUCTION

Microtextures—the size, shape, abundance, and interrelationship of crystals in a rock—record how metamorphic reactions proceed (Vernon, 1983). The identification of textures indicative of equilibrated (sub-) systems has led to the successful application of equilibrium thermodynamics to constrain metamorphic stages, ultimately forming the interpretation of a pressure (*P*)–temperature (*T*) path (see Lanari & Duesterhoeft, 2019 for a review). Conversely, reaction textures between several minerals (e.g. coronas and symplectites) or compositional zoning within individual minerals may indicate sluggish transformation of a previously equilibrated assemblage to a new equilibrium under different *P*–*T* conditions. These reaction textures contain valuable information about the kinetics of metamorphic reactions, including fluid–rock interaction processes (Carlson *et al.*, 2015).

Garnet is a useful mineral for metamorphic petrologists because it is stable in a wide range of bulk compositions and records the *P*–*T* conditions at which garnet grew (Caddick & Kohn, 2013), crystallization ages (Baxter *et al.*, 2017), growth processes (Ague & Carlson, 2013), and fluid pulses (Bovay *et al.*, 2021). Several studies have shown that garnet may be partially dissolved in reactions involving an internally or externally derived fluid (Foster, 1986; Whitney *et al.*, 1996; Dempster *et al.*, 2019; Wolfe *et al.*, 2021). Atoll-shaped garnets have been documented in multiple rock types, where garnet cores are replaced and embayed rims are preserved, resulting in unusual-shaped garnet crystals (e.g. Williamson, 1935; Atherton & Edmunds, 1966; Smellie, 1974). The following mechanisms are described in the literature to explain the formation of atoll-like garnet microtextures. Replacement of the original garnet core is proposed in cases where the atoll truncates the compositional zoning (Smellie, 1974; Homam, 2003; Cheng *et al.*, 2007; Faryad *et al.*, 2010). Multi-site nucleation followed by coalescence is suggested for garnets with complex zoning patterns (Spiess *et al.*, 2001; Dobbs *et al.*, 2003). Atolls consisting of very inclusion-rich domains are explained by rapid poikiloblastic growth (Atherton & Edmunds, 1966; Robyr *et al.*, 2014). Atoll garnet formation by replacement has been linked to fluid-related resorption when cores are replaced by hydrous products such as micas and amphiboles (Homam, 2003; Faryad *et al.*, 2010; Cao *et al.*, 2018; Giuntoli *et al.*, 2018). Atoll garnets formed by this final mechanism represent a promising texture for studying the kinetics of fluid-driven reactions.

Understanding the kinetics of fluid-driven reactions requires detailed petrography of the partial dissolution textures and quantification of their extent and distribution. Micro-computed tomography (μCT) allows micrometer-resolution imaging of 3D rock samples (Ketcham & Carlson, 2001). Statistical analysis of 3D data from garnet-bearing rocks has led to a quantitative description of porphyroblastic crystallization in metamorphic rocks (Kretz, 1974; Carlson & Denison, 1992; Hirsch *et al.*, 2000). Applying such methods to retrograde partial dissolution requires the examination of individual grain shapes to identify dissolved grains. This remains a laborious task for samples containing hundreds to

Received: November 23, 2023. **Revised:** January 15, 2024. **Accepted:** January 23, 2024

thousands of garnets, which has prevented petrographic analysis from transcending a qualitative description of retrogression-related textures. Computer vision techniques have been successfully applied in various fields to automate pattern, shape, or object recognition tasks (LeCun *et al.*, 2015). When applied to petrological μCT scans, this enables quantitative textural analysis of individual grain shapes on sample-scale garnet populations in 3D.

This study investigates garnet dissolution in a metabasalt from the Western Alps by studying the size, shape, and distribution of atoll garnets to unravel the kinetics of fluid-driven reactions that occur after garnet growth. GarNET, a deep learning classifier for grain shape, is presented for automating quantitative 3D petrography of garnet.

SAMPLE AND METHODS

Metabasalt ZS-21-02 is from the Zermatt–Saas zone (Western Alps), which has undergone eclogite-facies metamorphism (Angiboust *et al.*, 2009) during Alpine subduction (Rubatto *et al.*, 1998; Bovay *et al.*, 2022). The associated high-pressure mineral assemblage is partly preserved as coarse-grained relics of garnet, glaucophane, and clinozoisite. Paragonite and clinozoisite form pseudomorphs after lawsonite. Fine-grained aggregates of Na–Ca amphibole and plagioclase are interpreted as pseudomorphs after omphacite. The eclogite-facies relics are embedded in a partially retrogressed matrix of Na–Ca amphibole, plagioclase, clinozoisite, paragonite, phengite, calcite, and quartz (Fig. 1a). Inclusions in garnet mark an older rotated foliation in which porphyroblast crystallization was syn-kinematic. The pervasive matrix foliation is defined by elongated amphibole, clinozoisite and mica, and anastomoses around the pre-kinematic garnets. Rims of Na–Ca amphibole–plagioclase symplectites around glaucophane and chlorite around garnet are interpreted as products of late-stage low-pressure overprinting. Garnet is compositionally zoned with the cores relatively enriched in spessartine and grossular (Grt-core: $Alm_{40}Prp_{03}Sps_{21}Grs_{35}$; Fig. 1) and the rims relatively enriched in almandine and pyrope (Grt-rim: $Alm_{67}Prp_{10}Sps_{02}Grs_{22}$; Fig. 1). The composition of the core of smaller garnets matches that of an intermediate zone in larger garnets (Grt-mantle: $Alm_{59}Prp_{7}Sps_{3}Grs_{30}$; Fig. 1). An outermost discontinuous rim is characterized by increasing pyrope and low grossular content (Grt-outermost rim: $Alm_{64}Prp_{14}Grs_{20}Sps_{2}$). In the largest mapped garnet grain, the compositional zoning is truncated by the dissolution of the garnet core, forming the atoll garnet reaction texture (arrow in Fig. 1b). Atoll garnet interiors are locally replaced by clinozoisite, glaucophane, Na–Ca amphibole, paragonite, phengite, plagioclase, and quartz (Fig. 1a). Plagioclase and Na–Ca amphibole are interpreted to be secondary products of glaucophane decomposition under subsequent greenschist facies conditions. The relation between the atoll microtexture and the compositional zoning of garnet, and the hydrous replacement assemblage clearly shows atoll garnet formation by fluid-related resorption.

Compositional analysis

Quantitative compositional maps of garnet were obtained using electron probe micro-analysis and XMapTools (Lanari *et al.*, 2014, 2019). Bulk rock chemical analysis was conducted by measuring pressed powder pellets using laser ablation inductively coupled plasma mass spectrometry, following the procedure of Peters & Pettke (2017). A detailed description of the analytical methods can be found in Supplemental Material S1.

3D petrography

Cylindrical sample cores were imaged in 3D and at high resolution (3–18 μm) using μCT. A detailed description of the imaging, training dataset, training process, and performance analysis can be found in Supplemental Materials S1–S3. Garnet was isolated from the μCT scans by image segmentation using the software Dragonfly, Version 2022.2. Range selection in the X-ray absorption histogram was used to separate garnet and combined with morphological kernel operations to isolate garnet from noise and artifacts, e.g. mixed voxels between dense accessories and the matrix assemblage overlapping in absorption with the garnet. Single garnet grains were isolated from the segmented scans by connected component labeling using the algorithm of Silversmith (2021). Garnet grains were then pre-processed and classified into different shapes with the program garNET. During pre-processing, each 3D dataset of a single grain was reduced to a three-channel RGB image. The voxels of the 3D grain were summed up along each of the orthonormal coordinate axes. The resulting matrices holding those sums have each been saved in one of the three 8-bit channels of an RGB image (Fig. 2a). This pre-processing step reduces the 3D data of each individual grain to a single image while preserving information about the grain's outline shape and the internal mass distribution.

The pre-processed images encapsulating the grain shapes were then classified by a convolutional neural network (CNN). CNNs are a specific type of neural network (syn. deep learning) that are particularly powerful for computer vision tasks. The parameters of convolutional filters are optimized during the training to extract local image features and combine them into patterns useful for classification. The CNN in garNET consists of four blocks of 64 trainable three-by-three kernel convolutions, followed by two fully connected layers and a SoftMax output (Fig. 2b). The CNN was trained for 250 epochs on 6217 human-labeled images for the classes: Atoll, Pitted, Whole, Multiple, and Edge (Figs 2c and 3a). To create the training dataset, garnet grains were compiled from μCT scans of eight samples with different processes of atoll formation (Robyr *et al.*, 2014; Giuntoli *et al.*, 2018; Piccoli *et al.*, 2022; Rubatto *et al.*, 2023). For the performance validation, 15% of the data were withheld during training. Data augmentation was used on the remaining training data to reduce overfitting. The performance of the trained CNN was evaluated using the fully human-labeled μCT scan of sample ZS-21-02 as an independent test set. The overall accuracy of the CNN is 74%, and the macro-averaged F1 score (harmonic mean of precision and recall of each class) is 70%. The F1 score for atoll garnet detection is 69%. For samples with atoll garnet formation by replacement crystallization, a similar performance can be assumed. Caution is advised when grain shapes not represented in the training dataset are present, e.g. coalesced (atoll) garnet (Spiess *et al.*, 2001) or atoll garnets partly filled with reprecipitated garnet (Cheng *et al.*, 2007; Faryad *et al.*, 2010). Sampling and labeling a small test dataset allow the performance of garNET to be assessed before applying it to new samples, without the need to classify complete garnet populations.

MICROTEXTURES OF GARNET CRYSTALS

Three classes of garnet shape were distinguished in ZS-21-02 (Fig. 3a), whole garnets, atoll garnets, and pitted garnets. Whole garnets are subspherical grains with varying degrees of external resorption, from subhedral crystals to completely rounded grains, sometimes with minor concave resorption bays. Atoll garnets

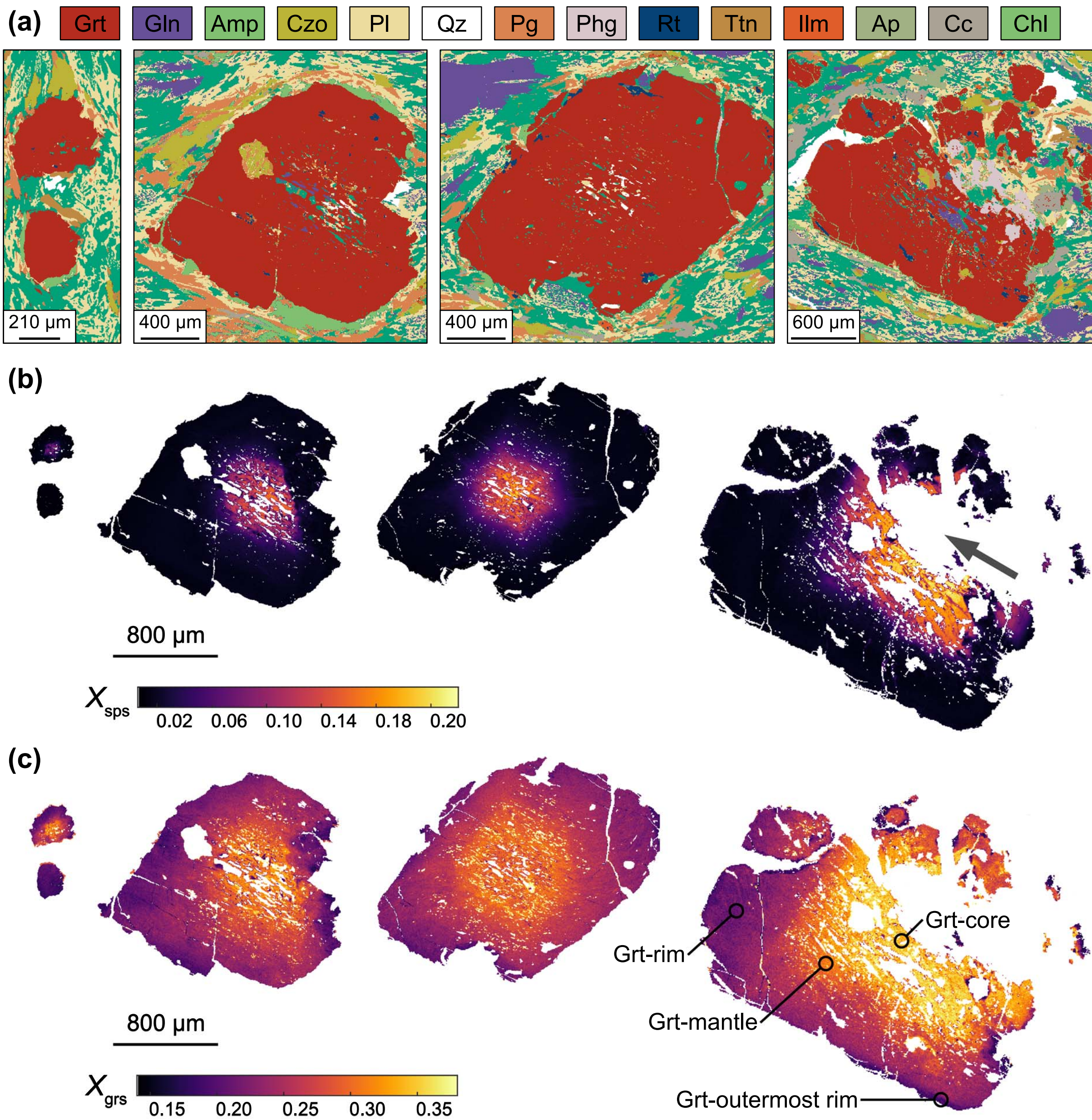

Fig. 1. Electron probe micro-analysis (EPMA) maps of sample ZS-21-02. (a) Mineral assemblage maps of four areas examined using EPMA. Mineral abbreviations after Warr (2021), except for Phengite (Phg). Compositional maps of the (b) spessartine (X_{sps}) and (c) grossular (X_{grs}) contents in garnet from the same four areas (adjusted for equal scale). Labels Grt-core, Grt-mantle, Grt-rim, and Grt-outermost rim denote different compositional zones in garnet. Note the truncation of the zoning pattern in the largest crystal by atoll-type dissolution marked by the arrow.

are grains with a replaced core and a remnant rim forming a hollow sphere. The central cavity is always connected to the rock matrix. This connection can be minimal, a needle-shaped tunnel, or up to an open cone cutting into the garnet core. These two shapes are end-member geometries, whereas natural grains show a spectrum of increasing degrees of atoll formation. To account for some of this continuity, pitted garnets are described as a discrete intermediate-shape class. This class is characterized by one or more deep needles or pits piercing the garnet but no visible excavation of the garnet core.

A total of 1841 grains were extracted from ZS-21-02, of which 1353 garnets remained for statistical analysis after filtering out artefactual geometries (e.g. multiple and edge intersecting grains). Atoll garnets comprise 21% of the garnet population, while 18% are pitted. The spatial distribution of garnet porphyroblasts in the sample ZS-21-02 follows an inclined foliation (Fig. 3b). Small variations in garnet abundance across the foliation are interpreted to result from microspatial variations in the bulk composition of the local equilibration volume during prograde garnet crystallization (Daniel & Spear, 1999). Atoll and pitted grains are uniformly distributed within the garnet population. There is no systematic association with the observed abundance variation, ruling out a scenario of resorption along fluid channels. The homogeneous distribution of atoll and pitted grains throughout the sample shows that garnet resorption was ubiquitous at the sample scale and indicates that a pervasive retrograde fluid passed through the rock.

The crystal size distribution (CSD) of garnet was estimated by fitting convex hulls around each porphyroblast (Bradford Barber et al., 1996) and then by calculating radii (r) from their volumes

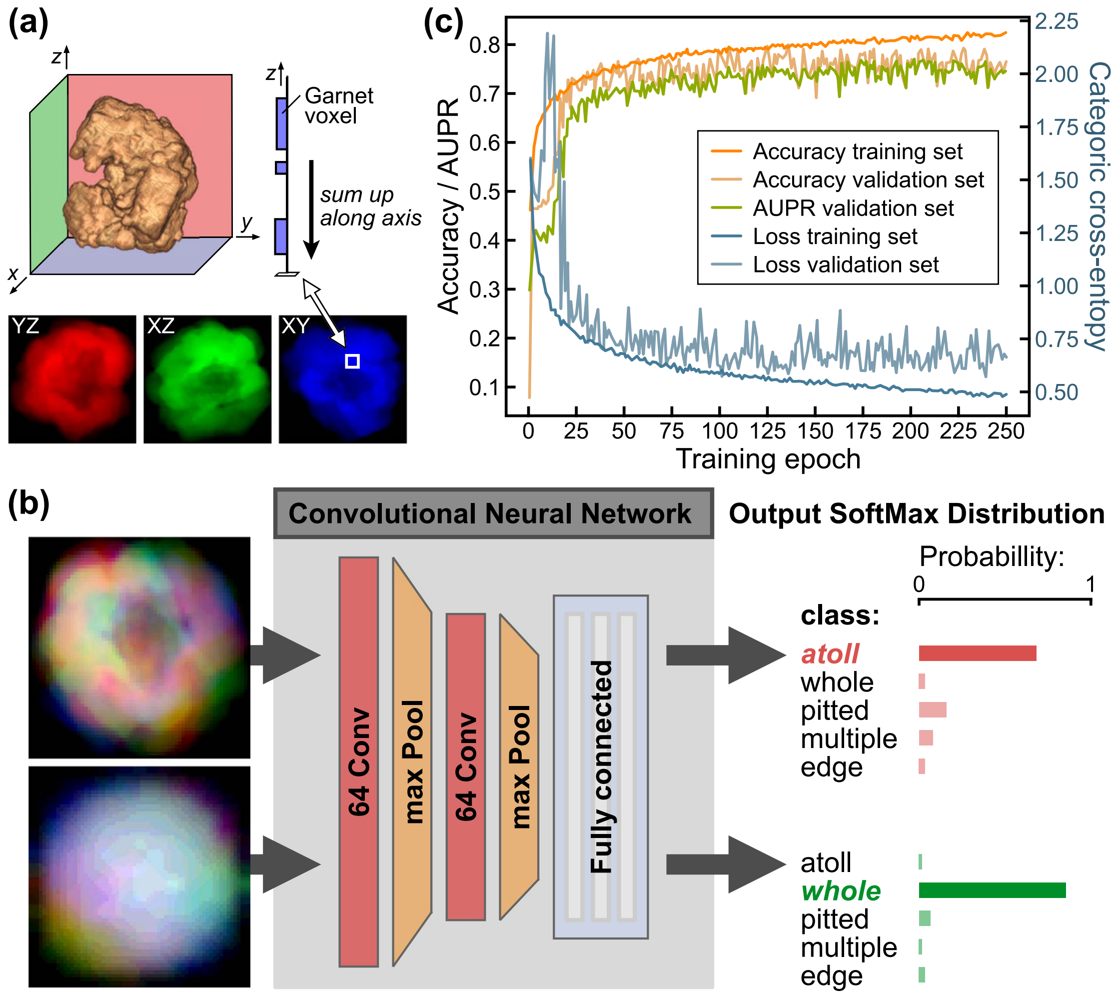

Fig. 2. Methodology for the automated classification of garnet grain shapes using garNET. (a) Pre-processing procedure to reduce the third-order tensors containing the 3D geometry of single grains to RGB images. For each pixel in the resulting images, the sum over the orthogonal coordinate axes is calculated and converted to an 8-bit RGB channel intensity. (b) Forward pass of a pre-processed grain image through the CNN resulting in a SoftMax probability distribution for the class predictions. (c) Training curves of the CNN showing the evolution over 250 training epochs for the performance metrics, accuracy, and area under the precision-recall curve (AUPR), and the categorical cross-entropy loss. The AUPR is averaged over all classes and used as a secondary metric that is less sensitive to class imbalance in the validation data.

assuming a spherical geometry. The resulting CSD for all garnets can be approximated by a log-normal distribution, which is bounded for spherical equivalent grain radii at 0.28 mm (Fig. 3c, Supplemental Material S4). The CSDs for atoll and pitted garnets are approximated by log-normal distributions shifted towards larger grain radii (note the logarithmic scale of the x-axis in Fig. 3c). The positive correlation between crystal size and interior resorption is confirmed by the increasing proportion of atoll and pitted garnets from <20% of the population in the smallest radius class of the CSD, to >60% in the largest radius class (blue and red curves in Fig. 3).

A CSD results from crystallization processes acting over time, where the nucleation rate determines the number of crystals added, and the growth rate determines the increase in crystal size within a time interval (Kretz, 1974). Assuming crystallization as a concatenation of stochastic sub-processes, a normal or, with the additional physical constraint of $r \geq 0$, a log-normal CSD follows from the central limit theorem. This log-normal distribution is consistent with the observed data. This is further supported by other empirical studies reporting normal (Kretz, 1993) and log-normal CSDs (Cashman & Ferry, 1988; Carlson *et al.*, 1995; Gaidies *et al.*, 2011). George & Gaidies (2017) showed that garnet crystallization can be modeled as a succession of equilibrium states through changing *P*, *T*, and reactive bulk composition. In a finite time interval, the stable garnet composition either grows onto existing porphyroblasts or nucleates to form new grains. The continuous growth and nucleation of garnet results in specific compositional zoning patterns for different size classes of a CSD. This aligns with the observed changes in the compositional zoning pattern for the differently sized garnets mapped in ZS-21-02, assuming that the garnets mapped in thin section are close to central sections through three-dimensional grains.

Crystal-size dependent compositional zoning patterns explain why larger garnets are more likely to be internally resorbed. The changes in core composition between different size classes are probably responsible for the observed differences in reactivity. Another factor that potentially influences the reactivity is the abundance of inclusions enlarging the reactive garnet surface. In ZS-21-02, this is ruled out because petrographic observations do not reveal a size dependency on the presence of inclusions. This makes composition a first-order variable controlling garnet dissolution rates during the retrogression of ZS-21-02.

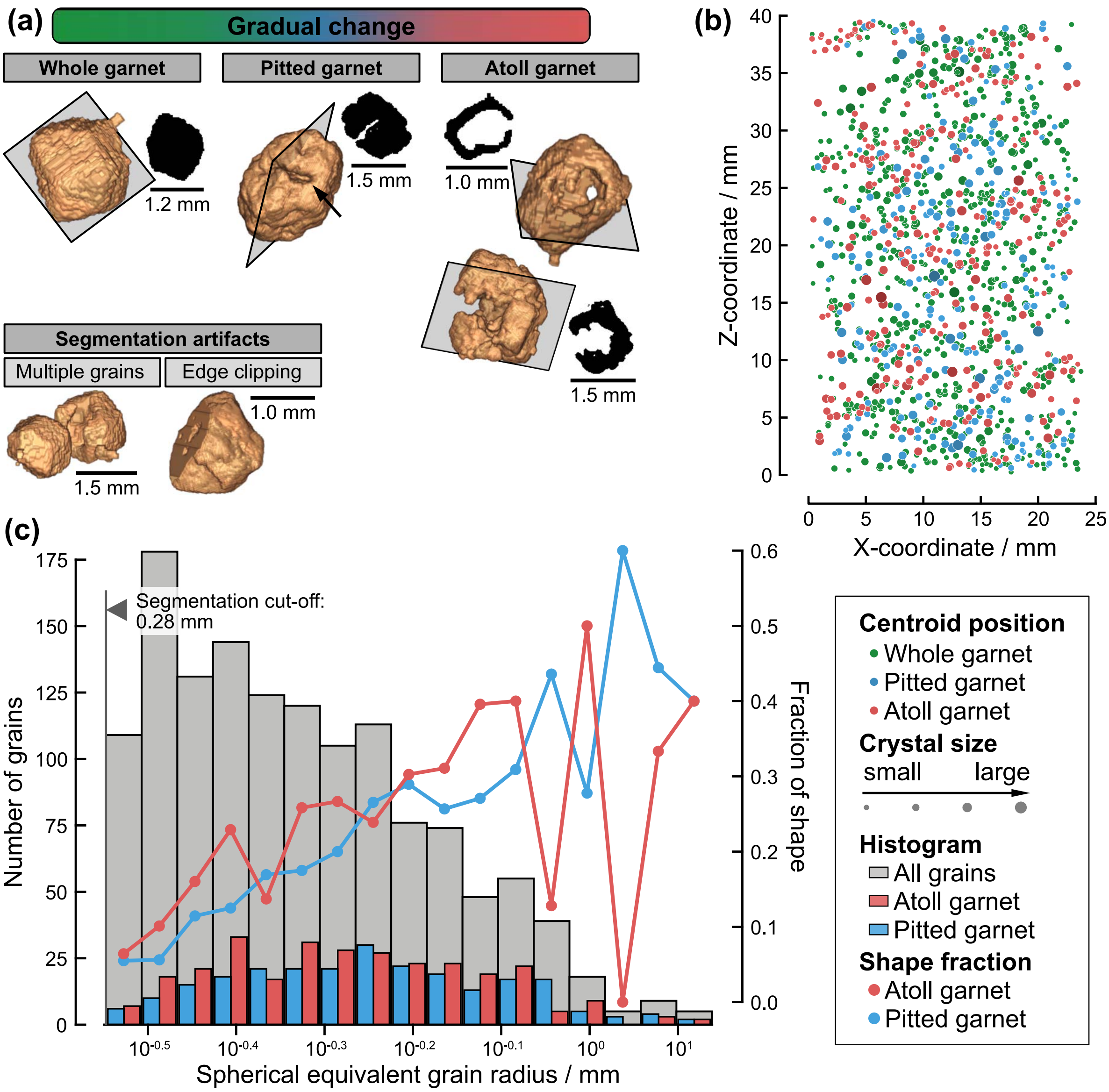

Fig. 3. Garnet grain shapes and distribution obtained using micro-computed tomography (μCT) and grain shape analysis. (a) Selection of garnet grain shapes. Three shape-based classes capture the gradual progression from whole garnets, with no evidence of internal resorption, to atoll garnets, with complete core dissolution. The μCT imaging and segmentation method results in other artefactual grain geometries; these are filtered from the dataset by classifying them into separate classes. (b) Microspatial distribution of garnet. Circles represent the centroid position of all whole, pitted, or atoll garnet grains ($r > 0.28$ mm) in ZS-21-02. Circle size is proportional to the grain size, and the colors differentiate the shape-based subpopulations. (c) CSD of the entire garnet population (gray), atoll garnet (red), and pitted garnet (blue) in ZS-21-02. Crystal size before resorption is estimated as a convex hull that fits the grain. The *x*-axis shows the grain size as spherical equivalent radius on a logarithmic scale. A second axis shows the fraction of grains in each size category that are atoll (red) and pitted (blue). Segmentation cut-off of 0.28 mm is highlighted by the vertical line.

KINETIC MODEL OF ATOLL GARNET FORMATION

The reaction rate of garnet dissolution can be expressed as (Lasaga, 1998, and references therein)

$$\upsilon = k_0 * \left(1 - e^{\frac{-E_a}{RT}}\right) * \left(1 - e^{\frac{\Delta G}{RT}}\right) \quad (1)$$

where the activation energy (E_a), temperature (T), and a Gibbs free energy change (ΔG) are the variables controlling the reaction rate (υ). The pre-exponential factor (k_0) and the ideal gas constant (R) are constants. For different metastable compositional zones of garnet, their difference in Gibbs free energy above the G-hyperplane (ΔG_{eq}), defined by the equilibrium assemblage, is considered as the ΔG driving the reaction (Fig. 4). It is not possible to determine the absolute reaction rates of garnet during the atoll formation, as the values of k_0 and E_a are unknown. However, the relative dissolution rate of the garnet core compared to its rim ($\upsilon_{core\text{-}rim}$) can be calculated assuming that E_a is the same for the two reactions. This assumes that garnet is the reactant whose slow dissolution kinetics control E_a and that a change in activation energy for garnet of different compositions is negligible in the observed compositional range. The relative rate obtained from Equation (1) is as follows:

$$\upsilon_{core-rim} = \frac{1 - e^{\Delta G_{eq}^{core}(RT)^{-1}}}{1 - e^{\Delta G_{eq}^{rim}(RT)^{-1}}} \quad (2)$$

The ΔG_{eq} was calculated using Theriak (de Capitani & Brown, 1987; de Capitani & Petrakakis, 2010) as the distance—expressed in joule per mole—between the Gibbs free energy of

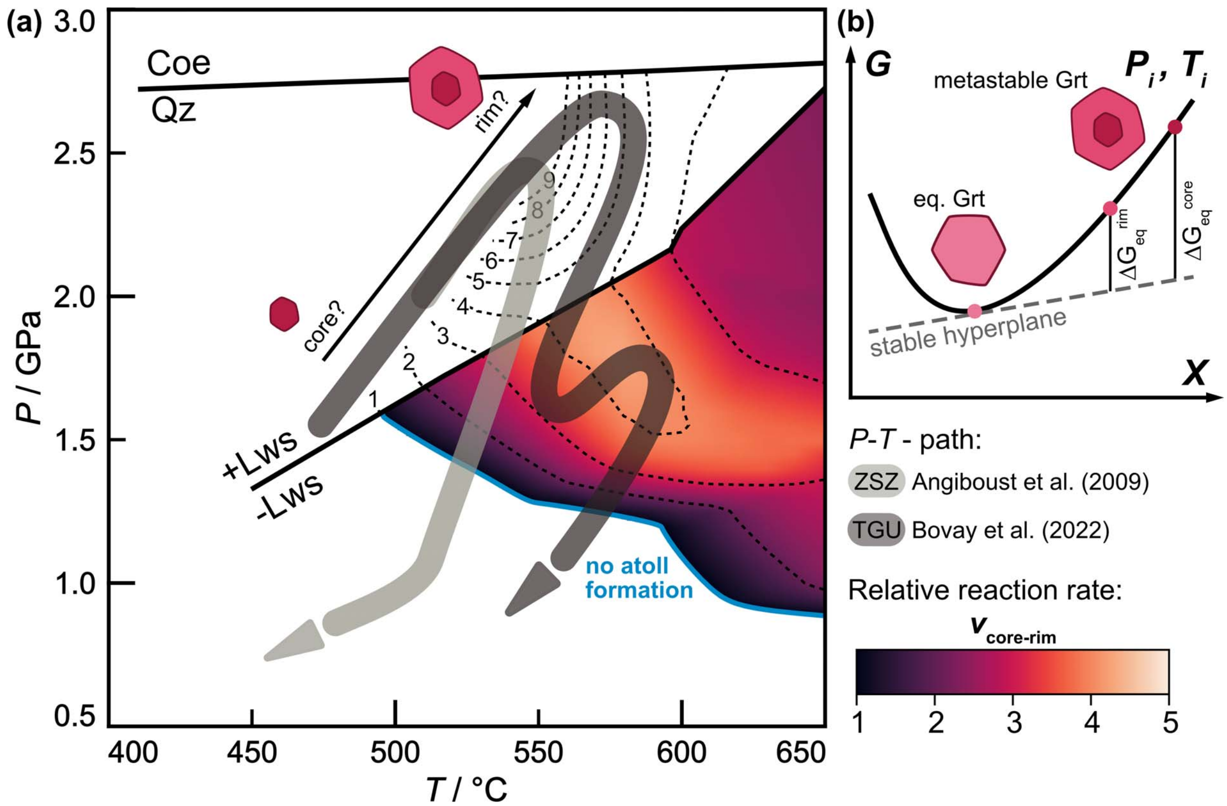

Fig. 4. Kinetic model of atoll garnet formation. (a) Map of the reaction rate of garnet core composition relative to garnet rim composition, $\nu_{core\text{-}rim}$, across *P–T*. A $\nu_{core\text{-}rim}$ of 1.0 results in equally rapid core and rim resorption, and higher values in increasingly rapid garnet core resorption. The *P–T* region below the blue line is where the rim is predicted to dissolve more rapidly, impeding atoll garnet formation. The lawsonite breakdown reaction is chosen as the upper limit of atoll garnet formation based on the replacing assemblage observed in the sample. In the lawsonite stability field, only contour lines of $\nu_{core\text{-}rim}$ are plotted. Reactions are extracted from a phase assemblage diagram calculated using Theriak-Domino and thermodynamic dataset ds5.5 (Holland & Powell, 1998). The highest $\nu_{core\text{-}rim}$ occur during initial decompression and overlap with a proposed heating pulse in the adjacent Theodul-Glacier Unit, which is not recognized in the Zermatt–Saas zone. (b) Schematic diagram of the driving force ΔG for atoll garnet formation. The equilibrium assemblage defines a *G*-hyperplane in compositional space (*X*) at fixed *P*, *T*. Each solution phase, a function *G*(*X*), tangents the hyperplane at the stable composition as shown for garnet in the diagram. Metastable phases of the same mineral (i.e. with a different composition) lie above the hyperplane. The distance between the metastable garnet core and rim to the hyperplane ΔG_{eq} is taken as energetic gradient controlling their reaction rate.

the garnet core and rim compositions and the *G*-hyperplane at the same compositions (Fig. 4). Maps of $\nu_{core\text{-}rim}$ in *P–T* space were calculated using the Python package pytheriak (Hartmeier & Lanari, 2023).

The differential reactivity $\nu_{core\text{-}rim}$ (Fig. 4) is modeled as the initial driving force towards equilibrium. The garnet's core and rim are metastable phases, and the reaction extent is at zero. Changing reaction rates with reaction progression are not accounted for by the model. At the *P–T* where the garnet rim is stable, the expression of $\nu_{core\text{-}rim}$ is undefined and asymptotically approaches infinity around this point. This results in a global maximum of $\nu_{core\text{-}rim}$ around the peak metamorphic conditions (Fig. 4). In rock samples where the garnet core is no longer fractionated from the system at peak conditions, this results in atoll formation close to peak metamorphic conditions (Cao *et al.*, 2018). In ZS-21-02, clinozoisite and paragonite in atoll garnets suggest that garnet remained fractionated from the reactive bulk composition within the lawsonite stability field. The model predicts that ν_{core} is three to five times higher than ν_{rim} at temperatures of 530–620°C and pressures of 1.2–2.0 GPa (Fig. 4). This limits garnet dissolution, leading to atoll formation to the early retrograde decompression of the Zermatt–Saas zone (Fig. 4, Angiboust *et al.*, 2009; Bovay *et al.*, 2022). In *P–T* domains where the garnet rim is predicted to react faster than its core ($\nu_{core\text{-}rim} \leq 1.0$), resorption is expected to proceed from the grain boundary inwards, and atoll-type resorption can be excluded (below the blue line in Fig. 4).

While this model can explain the relative reactivity of metastable garnet by differential forcing towards equilibrium, it does not account for differences in the energetic barrier of the E_a. An implication of this simplification is that the garnet core, typically assumed to be fractionated, must be brought back into full reactive contact with the rock matrix. Several processes that develop reactive pathways penetrating the garnet have been described: (1) tensile cracks in garnet due to fluid overpressure (Cao *et al.*, 2018), (2) diffusional re-equilibration along subgrain boundaries (Konrad-Schmolke *et al.*, 2007), and (3) inclusion-induced fracturing by differential expansion (Whitney, 1996). The observation of abundant radial cracks in garnet and the coincidence of atoll formation with initial decompression and fluids liberated by lawsonite breakdown suggest a combination of (1) and (3) as the mechanism in ZS-21-02.

Reopening of garnet by decompression and exposure to the fluids produced during is expected in meta-mafic rocks by processes (1) and (2) mentioned above. It is of particular interest that the exhumation trajectories of high-pressure rocks cross a ridge-shaped local maximum of $\nu_{core\text{-}rim}$ (Fig. 4). During initial decompression, the almandine-rich garnet rim of ZS-21-02 stays close to equilibrium, forming this topography of $\nu_{core\text{-}rim}$ (see

Fig. S4 in the Supplemental Material for the isopleths of garnet at equilibrium). This suggests that atoll-type resorption may be more common than is generally thought during the exhumation of hydrous eclogites. If the isopleth topography resulting in a local maximum of $\upsilon_{\text{core-rim}}$ is unique for garnets with prograde compositional zoning developed on a cold subduction *P–T* path, atoll garnet could be a diagnostic tool for detecting cold subduction in retrogressed mafic rocks, even when other evidence is lost due to overprinting. Further research will be needed to investigate the effect of *P–T* trajectories systematically and assess potential bulk rock compositional effects.

CONCLUSION

The homogeneous occurrence of atoll-type resorption within the garnet population supports a model of atoll garnet formation, in which the resorption is controlled internally, rather than by the limited or localized presence of aqueous fluids. The correlation found between internal resorption textures and crystal size suggests that compositional zoning patterns control the preferential dissolution of the garnet interiors. Differences in the chemical driving force (ΔG) between the composition of the earliest nucleated garnet, which forms the cores of the largest grains, and the later nucleated garnet rims, result in faster dissolution of the former.

This study highlights the potential of machine learning methods to automate repetitive and therefore time-consuming tasks in geological studies. To our knowledge, this is the first application of CNN-automated classification to petrographic analysis of crystal geometries in 3D. The presented data reduction scheme from 3D data to RGB images reduces network training time and allows for more stable loss conversion during training. Large datasets of crystal shapes with high variance will help to further increase the precision of deep learning classifiers and need to be used to test their generalization capabilities.

CNN-automated classification brings new quantitative approaches to traditionally descriptive disciplines such as petrography by providing large, statistically powerful datasets resolved for micro-textures of individual grains (Fig. 3). Linking these textural data to a kinetic model of $\upsilon_{\text{core-rim}}$ across *P–T* space provides a map of where atoll garnet formation is likely or suppressed (Fig. 4) and allows constraints to be placed on the partial retrogression during exhumation that is poorly recorded in compositional geochemical data.

Data availability

The data underlying this article are available in Zenodo, at https://doi.org/10.5281/zenodo.10073018. The code for the program garNET underlying this article is available on GitHub and archived in Zenodo, at https://doi.org/10.5281/zenodo.10201105.

Supplementary Data

Supplementary data are available at *Journal of Petrology* online.

Funding

This project has received funding from the European Research Council (ERC) under the European Union's Horizon 2020 research and innovation program [grant 850530] and from the Swiss National Science Foundation (SNSF) [grant IZSEZ0_210259].

Acknowledgements

We thank F. Picolli, L. Baumgartner, F. Giuntolli, and M. Tedeschi for providing samples. M. Tedeschi, H. Dominguez, R. Tamblyn, and A. Diwa are acknowledged for their assistance in the manual classification of garnet grain shapes. H. Cheng, F. George, and an anonymous reviewer are thanked for their insightful and constructive comments and C. Spandler for his efficient editorial handling.

References

Ague, J. J. & Carlson, W. D. (2013). Metamorphism as garnet sees it: the kinetics of nucleation and growth, equilibration, and diffusional relaxation. *Elements* **9**, 439–445. https://doi.org/10.2113/gselements.9.6.439.

Angiboust, S., Agard, P., Jolivet, L. & Beyssac, O. (2009). The Zermatt-Saas ophiolite: the largest (60-km wide) and deepest (c.70–80 km) continuous slice of oceanic lithosphere detached from a subduction zone? *Terra Nova* **21**, 171–180. https://doi.org/10.1111/j.1365-3121.2009.00870.x.

Atherton, M. P. & Edmunds, W. M. (1966). An electron microprobe study of some zoned garnets from metamorphic rocks. *Earth and Planetary Science Letters* **1**, 185–193. https://doi.org/10.1016/0012-821X(66)90066-5.

Baxter, E. F., Caddick, M. J. & Dragovic, B. (2017). Garnet: a rock-forming mineral petrochronometer. *Reviews in Mineralogy and Geochemistry* **83**, 469–533. https://doi.org/10.2138/rmg.2017.83.15.

Bovay, T., Rubatto, D. & Lanari, P. (2021). Pervasive fluid-rock interaction in subducted oceanic crust revealed by oxygen isotope zoning in garnet. *Contributions to Mineralogy and Petrology* **176**, 55. https://doi.org/10.1007/s00410-021-01806-4.

Bovay, T., Lanari, P., Rubatto, D., Smit, M. & Piccoli, F. (2022). Pressure–temperature–time evolution of subducted crust revealed by complex garnet zoning (Theodul Glacier Unit, Switzerland). *Journal of Metamorphic Geology* **40**, 175–206. https://doi.org/10.1111/jmg.12623.

Bradford Barber, C., Dobkin, D. P. & Huhdanpaa, H. (1996). The quickhull algorithm for convex hulls. *ACM Transactions on Mathematical Software* **22**, 469–483. https://doi.org/10.1145/235815.235821.

Caddick, M. J. & Kohn, M. J. (2013). Garnet: witness to the evolution of destructive plate boundaries. *Elements* **9**, 427–432. https://doi.org/10.2113/gselements.9.6.427.

Cao, D., Cheng, H., Zhang, L. & Wang, K. (2018). Origin of atoll garnets in ultra-high-pressure eclogites and implications for infiltration of external fluids. *Journal of Asian Earth Sciences* **160**, 224–238. https://doi.org/10.1016/j.jseaes.2018.04.030.

de Capitani, C. & Brown, T. H. (1987). The computation of chemical equilibrium in complex systems containing non-ideal solutions. *Geochimica et Cosmochimica Acta* **51**, 2639–2652. https://doi.org/10.1016/0016-7037(87)90145-1.

de Capitani, C. & Petrakakis, K. (2010). The computation of equilibrium assemblage diagrams with Theriak/Domino software. *American Mineralogist* **95**, 1006–1016. https://doi.org/10.2138/am.2010.3354.

Carlson, W. D. & Denison, C. (1992). Mechanisms of porphyroblast crystallization: results from high-resolution computed X-ray tomography. *Science* **257**, 1236–1239. https://doi.org/10.1126/science.257.5074.1236.

Carlson, W. D., Denison, C. & Ketcham, R. A. (1995). Controls on the nucleation and growth of porphyroblasts: kinetics from natural textures and numerical models. *Geological Journal* **30**, 207–225. https://doi.org/10.1002/gj.3350300303.

Carlson, W. D., Pattison, D. R. M. & Caddick, M. J. (2015). Beyond the equilibrium paradigm: how consideration of kinetics enhances metamorphic interpretation. *American Mineralogist* **100**, 1659–1667. https://doi.org/10.2138/am-2015-5097.

Cashman, K. V. & Ferry, J. M. (1988). Crystal size distribution (CSD) in rocks and the kinetics and dynamics of crystallization. *Contributions to Mineralogy and Petrology* **99**, 401–415. https://doi.org/10.1007/BF00371933.

Cheng, H., Nakamura, E., Kobayashi, K. & Zhou, Z. (2007). Origin of atoll garnets in eclogites and implications for the redistribution of trace elements during slab exhumation in a continental subduction zone. *American Mineralogist* **92**, 1119–1129. https://doi.org/10.2138/am.2007.2343.

Daniel, C. G. & Spear, F. S. (1999). The clustered nucleation and growth processes of garnet in regional metamorphic rocks from north-west Connecticut, USA. *Journal of Metamorphic Geology* **17**, 503–520.

Dempster, T. J., Gilmour, M. I. & Chung, P. (2019). The partial equilibration of garnet porphyroblasts in pelitic schists and its control on prograde metamorphism, Glen Roy, Scotland. *Journal of Metamorphic Geology* **37**, 383–399. https://doi.org/10.1111/jmg.12467.

Dobbs, H. T., Peruzzo, L., Seno, F., Spiess, R. & Prior, D. J. (2003). Unraveling the Schneeberg garnet puzzle: a numerical model of multiple nucleation and coalescence. *Contributions to Mineralogy and Petrology* **146**, 1–9. https://doi.org/10.1007/s00410-003-0488-4.

Faryad, S. W., Klápová, H. & Nosál, L. (2010). Mechanism of formation of atoll garnet during high-pressure metamorphism. *Mineralogical Magazine* **74**, 111–126. https://doi.org/10.1180/minmag.2010.074.1.111.

Foster, C. T. (1986). Thermodynamic models of reactions involving garnet in a sillimanite/staurolite schist. *Mineralogical Magazine* **50**, 427–439. https://doi.org/10.1180/minmag.1986.050.357.07.

Gaidies, F., Pattison, D. R. M. & de Capitani, C. (2011). Toward a quantitative model of metamorphic nucleation and growth. *Contributions to Mineralogy and Petrology* **162**, 975–993. https://doi.org/10.1007/s00410-011-0635-2.

George, F. R. & Gaidies, F. (2017). Characterisation of a garnet population from the Sikkim Himalaya: insights into the rates and mechanisms of porphyroblast crystallisation. *Contributions to Mineralogy and Petrology* **172**, 57. https://doi.org/10.1007/s00410-017-1372-y.

Giuntoli, F., Lanari, P. & Engi, M. (2018). Deeply subducted continental fragments—part 1: fracturing, dissolution–precipitation, and diffusion processes recorded by garnet textures of the central Sesia zone (western Italian Alps). *Solid Earth* **9**, 167–189. https://doi.org/10.5194/se-9-167-2018.

Hartmeier, P. & Lanari, P. (2023). *pytheriak (v.1.1.0)*. Zenodo. https://doi.org/10.5281/zenodo.7945481.

Hirsch, D. M., Ketcham, R. A. & Carlson, W. D. (2000). An evaluation of spatial correlation functions in textural analysis of metamorphic rocks. *Geological Materials Research* **2**, 1–42.

Holland, T. J. B. & Powell, R. (1998). An internally consistent thermodynamic data set for phases of petrological interest. *Journal of Metamorphic Geology* **16**, 309–343. https://doi.org/10.1111/j.1525-1314.1998.00140.x.

Homam, S. M. (2003). Formation of atoll garnet in the Ardara aureole, NW Ireland. *Journal of Sciences, Islamic Republic of Iran* **14**, 247–258.

Ketcham, R. A. & Carlson, W. D. (2001). Acquisition, optimization and interpretation of X-ray computed tomographic imagery: applications to the geosciences. *Computers & Geosciences* **27**, 381–400. https://doi.org/10.1016/S0098-3004(00)00116-3.

Konrad-Schmolke, M., O'Brien, P. J. & Heidelbach, F. (2007). Compositional re-equilibration of garnet: the importance of sub-grain boundaries. *European Journal of Mineralogy* **19**, 431–438. https://doi.org/10.1127/0935-1221/2007/0019-1749.

Kretz, R. (1974). Some models for the rate of crystallization of garnet in metamorphic rocks. *Lithos* **7**, 123–131. https://doi.org/10.1016/0024-4937(74)90025-5.

Kretz, R. (1993). A garnet population in Yellowknife schist, Canada. *Journal of Metamorphic Geology* **11**, 101–120. https://doi.org/10.1111/j.1525-1314.1993.tb00134.x.

Lanari, P. & Duesterhoeft, E. (2019). Modeling metamorphic rocks using equilibrium thermodynamics and internally consistent databases: past achievements, problems and perspectives. *Journal of Petrology* **60**, 19–56. https://doi.org/10.1093/petrology/egy105.

Lanari, P., Vidal, O., De Andrade, V., Dubacq, B., Lewin, E., Grosch, E. G. & Schwartz, S. (2014). XMapTools: a MATLAB©-based program for electron microprobe X-ray image processing and geothermobarometry. *Computers & Geosciences* **62**, 227–240. https://doi.org/10.1016/j.cageo.2013.08.010.

Lanari, P., Vho, A., Bovay, T., Airaghi, L. & Centrella, S. (2019). Quantitative compositional mapping of mineral phases by electron probe micro-analyser. *Geological Society, London, Special Publications* **478**, 39–63. https://doi.org/10.1144/SP478.4.

Lasaga, A. C. (1998) *Kinetic Theory in the Earth Sciences*. Princeton: Princeton University Press.

LeCun, Y., Bengio, Y. & Hinton, G. (2015). Deep learning. *Nature* **521**, 436–444. https://doi.org/10.1038/nature14539.

Peters, D. & Pettke, T. (2017). Evaluation of major to ultra trace element bulk rock chemical analysis of nanoparticulate pressed powder pellets by LA-ICP-MS. *Geostandards and Geoanalytical Research* **41**, 5–28. https://doi.org/10.1111/ggr.12125.

Piccoli, F., Lanari, P., Hermann, J. & Pettke, T. (2022). Deep subduction, melting, and fast cooling of metapelites from the Cima Lunga Unit, Central Alps. *Journal of Metamorphic Geology* **40**, 121–143. https://doi.org/10.1111/jmg.12621.

Robyr, M., Darbellay, B. & Baumgartner, L. P. (2014). Matrix-dependent garnet growth in polymetamorphic rocks of the Sesia zone, Italian Alps. *Journal of Metamorphic Geology* **32**, 3–24. https://doi.org/10.1111/jmg.12055.

Rubatto, D., Gebauer, D. & Fanning, M. (1998). Jurassic formation and Eocene subduction of the Zermatt-Saas-Fee ophiolites: implications for the geodynamic evolution of the Central and Western Alps. *Contributions to Mineralogy and Petrology* **132**, 269–287. https://doi.org/10.1007/s004100050421.

Rubatto, D., Williams, M., Markmann, T. A., Hermann, J. & Lanari, P. (2023). Tracing fluid infiltration into oceanic crust up to ultra-high-pressure conditions. *Contributions to Mineralogy and Petrology* **178**, 79. https://doi.org/10.1007/s00410-023-02060-6.

Silversmith, W. (2021). *cc3d: Connected Components on Mutlilabel 3D & 2D Images (v3.12.3)*. Zenodo. https://doi.org/10.5281/zenodo.5535250.

Smellie, J. A. T. (1974). Formation of atoll garnets from the aureole of the Ardara pluton, Co. Donegal, Ireland. *Mineralogical Magazine* **39**, 878–888. https://doi.org/10.1180/minmag.1974.039.308.07.

Spiess, R., Peruzzo, L., Prior, D. J. & Wheeler, J. (2001). Development of garnet porphyroblasts by multiple nucleation, coalescence and boundary misorientation-driven rotations. *Journal of Metamorphic Geology* **19**, 269–290.

Vernon, R. H. (1983) *Metamorphic Processes*. Dordrecht: Springer Netherlands.

Warr, L. N. (2021). IMA–CNMNC approved mineral symbols. *Mineralogical Magazine* **85**, 291–320. https://doi.org/10.1180/mgm.2021.43.

Whitney, D. L. (1996). Garnets as open systems during regional metamorphism. *Geology* **24**, 147. https://doi.org/10.1130/0091-7613(1996)024%3C;0147:GAOSDR%3E;2.3.CO;2.

Whitney, D. L., Mechum, T. A., Dilek, Y. & Kuehner, S. M. (1996). Modification of garnet by fluid infiltration during regional metamorphism in garnet through sillimanite-zone rocks, Dutchess County, New York. *American Mineralogist* **81**, 696–705. https://doi.org/10.2138/am-1996-5-617.

Williamson, W. O. (1935). The composite gneiss and contaminated granodiorite of Glen Shee, Perthshire. *QJGS* **91**, 382–422. https://doi.org/10.1144/GSL.JGS.1935.091.01-04.14.

Wolfe, O. M., Spear, F. S. & Harrison, T. M. (2021). Pronounced and rapid exhumation of the Connecticut Valley trough revealed through quartz in garnet Raman barometry and diffusion modelling of garnet dissolution–reprecipitation reactions. *Journal of Metamorphic Geology* **39**, 1045–1069. https://doi.org/10.1111/jmg.12601.